Optimization of a smart beam for monitoring a connected inaccessible mechanical system: Application to bone-implant coupling

Anne-Sophie Poudrel, Vu-Hieu Nguyen, Guillaume Haiat, Giuseppe Rosi

Optimization of a smart beam for monitoring a connected inaccessible mechanical system : application to bone-implant coupling

Anne-Sophie Poudrel[a], Vu-Hieu Nguyen[b], Guillaume Haiat[a], Giuseppe Rosi[b]

[a] *CNRS, Univ Paris Est Creteil, Univ Gustave Eiffel, UMR 8208, MSME, F-94010 Créteil, France*
[b] *Univ Paris Est Creteil, Univ Gustave Eiffel, CNRS, UMR 8208, MSME, F-94010 Créteil, France*

Abstract

This paper deals with the optimization of piezoelectric patches positioning on a beam attached to an inaccessible system. Based on the electro-mechanical coupling coefficients, which are calculated from the mode shapes curvatures, the problem is to provide an optimal positioning of the piezoelectric patches in order to target the modes sensitive to beam boundary conditions. Following the theoretical description of a beam instrumented with collocated piezoelectric patches, a placement optimization strategy is proposed. This strategy lies on the definition of utility functions, based on modal weights and modal sensitivities, calculated from the coupling coefficient. An experimental validation of the method is performed on a concrete case study corresponding to real-time implant stability monitoring. A beam is temporarily rigidly fixed to the implant during its insertion into the bone cavity to allow impaction by the surgeon. The positions of the sensors on the beam are optimized to focus on the beam's modes carrying information on the bone-implant interface, the biomechanical issue being the real-time maximization of implant stability. The originality of the approach lies on the sensor placement optimization on the beam connected to the implant to maximize or minimize simultaneously the amplitude of several modes on the frequency response function at resonances, depending on their sensitivity to the bone-implant interface. The results show very good performance of the piezoelectric placement strategy proposed in this paper, paving the way for new applications of piezoelectric patches design and placement on structures.

Keywords: electro-mechanical coupling, piezoelectric patch optimization, mode observability, smart device, boundary conditions monitoring, bone-implant coupling

1. Introduction

Piezoelectric ceramic transducers bonded to flexible structures are widely employed in the context of dynamic measurements. They offer the advantage to be used as sensors or actuators due to to their property to convert mechanical strains into electrical voltage and *vice versa*. The modal electro-mechanical coupling

factors (MEMCF) [1, 2] associated to one piezoelectric patch and one mode of vibration of the structure is determinant for vibration reduction control [3].

In the literature, there are several examples of multi-modal control, either active or passive with shunted piezoelectric patches on beams [4, 5, 6] and plates [7, 8, 9]. For these applications, the piezoelectric patches are generally uniformly distributed on the structure, considering that every mode has the same weight and the optimization concerns the associated electric circuit. However, in specific applications, the design constraints limit the number of sensor/actuator patches over the structure. Therefore, another strategy for vibration reduction lies in the optimization of the placement and the design of the piezoelectric patch on the structure, as presented in the exhaustive review of Gupta et al. [10]. Among the different criteria used in the literature, maximizing the degree of mode controllability and observability are of particular interest. For instance, Ducarne et al. [11] proposed a parametric study on the placement and geometry of the patches in order to maximize the electro-mechanical coupling coefficient of one specific mechanical vibration mode, to which the shunt is tuned. Others authors studied the same problematic of placement optimization, by considering active control [12, 13]. Moreover, Halim and Moheimani [14] addressed the notions of both spatial and modal controllability, to find the optimal locations of piezoelectric transducers on the plate. The procedure is based on the concept of the spatial $\mathcal{H}$ norm, used to describe the spatial structural response of the system in an average sense. The optimization relies on the simultaneous vibration reduction over the entire structure, while maintaining modal controllability and observability of the selected vibration modes.

In this paper, the specific issue of optimizing the *observability* of a set of modes sensitive to the beam boundary conditions is addressed. Lots of vibro-acoustic applications are concerned by this issue, and among them, this paper focus on a biomedical application. In the orthopedic field, several methods are under development to assist and guide the surgeon during implant insertion into the bone, in order to achieve an optimal implant stability, corresponding to maximizing implant surrounding stresses while avoiding bone fracture risk. Among the different techniques, vibration measurement have proven to be efficient to monitor implant insertion into the bone [15, 16, 17]. Nevertheless, the fixation of sensors or probes on the implant and/or the bone is incompatible with a clinical application [18]. Therefore, several authors studied directly the vibrations of a square shape structure, named ancillary, and used by the surgeon to insert the implant into the bone [19, 20], which can easily be equipped with sensors and allow a good accessibility for measurement. This structure has one free extremity and another one bonded to the implant during its insertion. Due to this fixation, a previous study by our group showed that specific modes of vibration of this square beam structure carry information on the bone-implant system, and in particular on the system rigidity [20]. The

issue is then to propose an optimization approach for piezoelectric patch positioning on the square beam structure, in order to maximize or minimize the *observability* of the modes, depending on their sensitivity to the implant stability.

Several authors studied the piezoelectric placement optimization in order to target specific modes of interest. For instance, Rosi et al. [21] developed a similar transducer optimization approach for reducing the radiated sound power of thin plates produced by a set of modes. In the field of structural health monitoring, the position of the collocated piezoelectric transducers can be optimized in order to detect damage in thin plate-like structures based on the minimization of the Bayes risk [22]. Interestingly, not only the position but also the local beam stiffness could be adjusted by using the feedback voltage output from the piezoelectric sensors to tune the natural vibration of mode shape sensitive to the existence of a crack [23, 24]. In these examples, the criteria of mode selection differs from the sensitivity to beam boundary conditions. Moreover, in our study, the piezoelectric patches are not shunted since they are used as sensors and not for control purpose. As only the position of the patch on the beam is studied, no optimization algorithm are needed, contrary to what is often done for passive control applications [25, 26, 27]. Eventually, methods for boundary force measurement in beam-like structures have been investigated in the literature by displacement measurement [28] or distributed sensor measurement [29]. However, the issue of our application is to monitor implant stability throughout specific resonance frequency rather than boundary forces measurement.

The originality of the present paper comes from the use of an optimization method, based on the modal electro-mechanical coupling factor (MEMCF), in order to maximize the *observability* of a subset of modes sensitive to the beam boundary conditions, related to the implant stability for the considered case study. The choice of this application comes from the need to maximize the initial fixation of orthopedic implants during their insertion into the bone, which is one of the main biomechanical issues related to this surgery. Since this fixation is tricky to maximize for the surgeon without creating a bone fracture, some quantitative methods are underdevelopment to measure in real time implant stability. Some of them are based on the vibro-acoustic characterization of the bone-implant system [17, 30, 20]. In particular, the results of [20], which showed that the implant stability is correlated to specific resonance frequencies of the surgical tool used to insert the implant, named “ancillary” and assimilated to a beam with one free extremity and the other one bounded to the implant being inserted. To improve the vibration measurement method for implant stability characterization by focusing on specific modes of interest, optimal patches positions are determined hereafter on the beam which has one free extremity and the other bounded to the implant being inserted.

The paper is organized in two main sections. Section 2 is dedicated to the description of the smart

beam electromechanical behavior and to the transducers position optimization strategy based on mode *observability*. In particular, the modal electromechanical coupling between the patch and the beam and the utility functions chosen for the optimization of a subset of modes are defined. In Section 3, an experimental validation of the optimization strategy for implant insertion monitoring is carried out.

2. Equations of the smart device

2.1. Geometry and kinematics

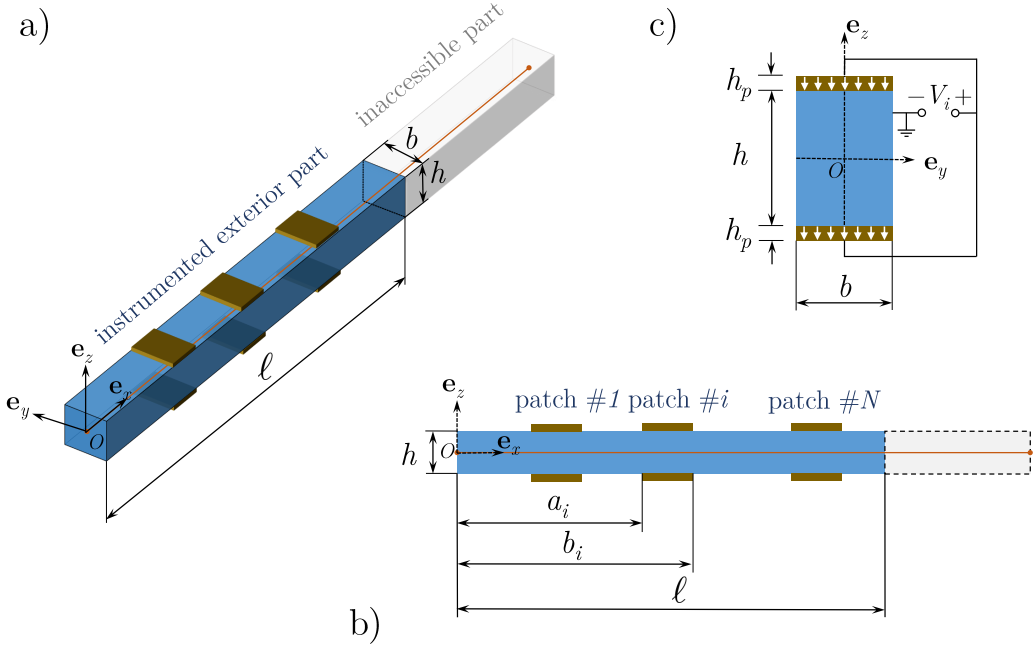

Figure 1: a) Geometry of the beam and connection with the inaccessible system b) Piezoelectric patches positions and numbering on the beam and c) A section containing i-th patches couple and the associated electric circuit with V_i the potential difference measured by each patches couple i

Consider an elastic beam of length ℓ with a rectangular section $b \times h$ (Fig. 1a), on which piezoelectric layers are bonded at n_p segments along its longitudinal axis x. The beam is fixed at $x_1 = \ell$ to an external mechanical system. At a segment $x \in [a_i, b_i]$ $(i = 1..n_p)$, the beam is sandwiched between two identical piezoelectric patches of thickness h_p which are put symmetrically at the upper and the lower surfaces of the beam (i.e at $z = h/2$ and $z = -h/2$) (Fig. 1b). Each couple of piezoelectric layers is polarized along $-\boldsymbol{e}_z$ (Fig. 1c) and thus form a pure bending sensor/actuator.

We assume the piezoelectric layers have the same width b with the beam's section. Each piezoelectric layer is covered on both its upper and lower surfaces by electrodes which are equipotential surfaces. The

electric field $\boldsymbol{E}$ assumed to be constant, uniform and parallel to the transverse direction $\boldsymbol{e}_z$, is : $E_z = -V/h_p$, where V the voltage applied between the electrodes. The purely elastic part of the beam is grounded.

In this study, all forces acting along $\boldsymbol{e}_y$ are neglected, the system may be described by a 1D Euler-Bernouilli model in the plane (x, z). Moreover, by assuming that the longitudinal and rotation of the beam are negligible, only flexural movement is considered. All components of the displacement field at a point of coordinates (x, y, z) may expressed in terms of the transverse displacement $w(x)$ of the beam's neutral axis:

$$u_x(x, y, z, t) = -zw'(x, t) \tag{1}$$

$$u_y(x, y, z, t) = 0 \tag{2}$$

$$u_z(x, y, z, t) = w(x, t) \tag{3}$$

2.2. Consitutive law and governing equations

By using the Euler-Bernoulli beam model, the transverse stress σ_{zz} and the shear strain ϵ_{xz} are negligible. Consequently, the only non-zero strain component is: $\epsilon_{xx} = u'_x = -zw''$ and the full piezoelectric constitutive equation (see Appendix A) reduces to:

$$\sigma_{xx} = Y\epsilon_{xx} - e_{31}E_z, \tag{4}$$

$$D_z = e_{31}\epsilon_{xx} + \varepsilon_{33}E_z. \tag{5}$$

At a point located in the elastic beam (i.e. for $z \in [-h/2, h/2]$): $Y = Y_b$, $\rho = \rho_b$, $e_{31} = 0$ and $\varepsilon_{33} = 0$. Otherwise, in the piezoelectric patches, the mechanical parameters are denoted by $\rho = \rho_p$ and $Y = Y_p$. Since piezoelectric ceramics are transversely isotropic, the elastic parameter Y_p is an in-plane Young modulus obtained from the corresponding complete elasticity tensor $\boldsymbol{c}$ using the following relation (see Appendix A:

$$Y_p = \frac{(c_{11} - c_{12})((c_{11} + c_{12})c_{33} - 2c_{13}^2)}{c_{11}c_{33} - c_{13}^2} \tag{6}$$

In the following, the extended Hamilton principle will be used for obtaining the equations of motion and continuity conditions [31]. See Appendix B for more details.

2.2.1. Equations in a segment containing i-th patch ($x \in [a_i, b_i]$)

With the presence of the upper and lower piezoelectric patches, the beam has three layers and the kinetic variation δT^* may be expressed by:

$$\delta T^* = \int_{a_i}^{b_i} \left(\int_{-b/2}^{b/2} \int_{-H/2}^{H/2} \rho(\delta \dot{w})\ \dot{w}\, dydz \right) dx = \int_{a_i}^{b_i} \bar{m}\ \delta \dot{w}\ \dot{w} dx, \tag{7}$$

where $H = h/2 + h_p$ and $\bar{m} = b(\rho_b h + 2\rho_p h_p)$ which is effective mass par unit length of the beam.

Similarly, by recalling that the electric potential is fixed ($\delta \boldsymbol{E} = 0$) and by substituting Eqs. (1-5) into (B.10), the potential variation δW_e^* reads:

$$\delta W_e^* = \int_{a_i}^{b_i} \left(\int_{-b/2}^{b/2} \int_{-H/2}^{H/2} (-\delta \epsilon_{xx}\ \sigma_{xx})\, dydz \right) dx \tag{8}$$

$$= \int_{a_i}^{b_i} \delta w''\ (-\mathcal{D}\ w'' + \mathcal{G} V)\ \ dx, \tag{9}$$

where

$$\mathcal{D} = \int_{-b/2}^{b/2} \int_{-H/2}^{H/2} Y z^2\ dydz = Y_b\ \frac{bh^3}{12} + Y_p\ \frac{bh_p(3h^2 + 6hh_p + 4h_p^2)}{6}, \tag{10}$$

$$\mathcal{G} = \int_{-b/2}^{b/2} \int_{-H/2}^{H/2} \frac{e_{31} z}{h_p}\ dydz = e_{31}\ b(h + h_p) = b\,(h + h_p)\, d_{31} Y_p, \tag{11}$$

are a bending stiffness and a coupling coefficient, respectively.

Then, integrating δW_e^* by parts twice with respect to x gives:

$$\delta W_e^* = \int_{a_i}^{b_i} \delta w\,(-\mathcal{D}\ w'' + \mathcal{G} V)''\ \ dx - \left[\delta w'\,(-\mathcal{D}\ w'' + \mathcal{G} V_i)\right]_{a_i}^{b_i} + \left[\delta w\,(-\mathcal{D}\ w'' + \mathcal{G} V_i)'\right]_{a_i}^{b_i} \tag{12}$$

$$= \int_{a_i}^{b_i} \delta w M'' dx - \left[\delta w' M\right]_{a_i}^{b_i} + \left[\delta w M'\right]_{a_i}^{b_i} \tag{13}$$

where $M := -\mathcal{D}\ w'' + \mathcal{G} V$ is the bending moment in the beam.

If we only consider a distributed transverse load $p(x,t)$ applied to the beam, the virtual work of external force is:

$$\delta W_{ext}^* = \int_{a_i}^{b_i} \delta w\ p\ dx. \tag{14}$$

In order to add the non conservative effects due to the internal damping of the beam, an extended Hamilton principle approach has to be used:

$$\int_{t_1}^{t_2} (\delta T^* + \delta W_e^* + \delta W_{ext} + \delta W_{nc}) = 0 \tag{15}$$

where δW_{nc} is the work expended by the the non conservative actions. In the case of internal damping of the beam, we suppose the existence of a linear velocity dependent action and this term reads:

$$\delta W_{nc} = -\int_0^\ell \eta w \delta \dot{w} dx \tag{16}$$

Finally, by applying the extended Hamilton's principle, the equations of motion reads:

$$\bar{m}\ddot{w} + \eta\dot{w} - M'' = p \tag{17}$$

along with the following continuity conditions, where $[\![f(x)]\!] = f(x^+) - f(x^-)$ is a jump function:

$$[\![w]\!] = 0, \qquad \text{(continuity of displacement)}, \tag{18}$$

$$[\![w']\!] = 0, \qquad \text{(continuity of rotation)}, \tag{19}$$

$$[\![\mathcal{D}\ w'' + \mathcal{G}V_i]\!] = 0, \qquad \text{(continuity of moment)}, \tag{20}$$

$$[\![(\mathcal{D}\ w'' + \mathcal{G}V_i)']\!] = 0, \qquad \text{(continuity of shear force)}. \tag{21}$$

As the piezoelectric patch is very thin with respect to the beam, the flexural rigidity $\mathcal{D}$ and the mass per unit length $\bar{m}$ of the beam, can be considered as uniform in $[0, \ell]$. In addition, the strain may be regarded as uniform over its thickness $\epsilon_{xx} = -z_m w''$ where $z_m = (h + h_p)/2$ is the coordinate of center line of the piezoelectric patch. The charge Q_i of the i-th patch is defined as the free electric contained electrode area [11]:

$$Q_i = b\int_{a_i}^{b_i} -D_z\ dx = b\int_{a_i}^{b_i} (e_{31} z_m w'' - \varepsilon_{33} E_z)\ dx \tag{22}$$

$$= \mathcal{G}(w'(b_i) - w'(a_i)) + C_i V_i \tag{23}$$

where $C_i = \varepsilon_{33} b(b_i - a_i)/h_p$. If the piezoelectric segment is left open-circuited, then $Q_i = 0$ and:

$$C_i V_i = -\mathcal{G}(w'(b_i) - w'(a_i)) \tag{24}$$

2.2.2. Equation for the whole domain ($x \in [0, \ell]$)

For describing the behavior of the beam with length ℓ with n_p patches, one may use the same expression of the equation (17), with a more general formulation of bending moment:

$$M = -\mathcal{D}w'' + \sum_{i=1}^{n_p} \mathcal{G}V_i(H(x - a_i) + H(x - b_i)), \quad x \in [0, \ell]. \tag{25}$$

where $H(.)$ denotes the Heaviside function.

Moreover, considering the beam with one free extremity and the other mechanically connected to another mechanical system, the boundary conditions at $x_1 = 0$ and $x_1 = \ell$ are:

$$w''(0) = 0, \qquad \text{(no bending moment on the free end)}, \tag{26}$$

$$w'''(0) = 0, \qquad \text{(no shear force on the free end)}, \tag{27}$$

$$\mathcal{D}\ w''(\ell) = M_{ext}, \qquad \text{(bending moment imposed by the external mechanical system)}, \tag{28}$$

$$\mathcal{D}\ w'''(\ell) = T_{ext}, \qquad \text{(shear force imposed by the external mechanical system)}. \tag{29}$$

2.3. Modal expansion

The harmonic motion of the beam may be expressed by N short-circuit eigenmodes $\omega_k, \phi_k(x)$ $(i = 1..N)$:

$$w(x, t) = \sum_{k=1}^{N} \phi_k(x) q_k(t) \tag{30}$$

where $q_k(t)$ is a time-dependant function. $\omega_k, \phi_k(x)$ may solved from by Eq. (17) with $p = 0$ and $V = 0$:

$$-\omega_k^2 \bar{m} \phi_k + \mathcal{D}\phi_k^{(4)} = 0 \tag{31}$$

where $^{(4)}$ represents the fourth derivative with respect to the coordinate x. The modes ϕ_k are orthogonal and may be normalized by:

$$\int_0^\ell \phi_j(x)\phi_k(x) = \delta_{jk} \tag{32}$$

By substituting (30) into (25), (17) , and multiplying the results by ϕ_j, one obtains N equations ($j = 1..N$):

$$\bar{m}\ddot{q}_j(t) + \omega_j^2 \bar{m} q_j(t) + \eta_j \dot{q}_j - \sum_{i=1}^{n_p} g_{ij} V_i = F_j \tag{33}$$

where $F_j = \int_0^\ell \phi_j p(x,t)\ dx$.

The value of the coupling coefficient g_{ij} of the patch i with respect to the mode j is defined by:

$$g_{ij}(a_i, b_i) = \mathcal{G} \int_{a_i}^{b_i} {\phi_j}''(x) dx = \mathcal{G}\left(\phi_j'(b_i) - \phi_j'(a_i)\right) \tag{34}$$

Similarly, substituting (30) into (24) leads to n_p equations ($i = 1..n_p$):

$$C_i V_i + \sum_{j=1}^{N} g_{ij} q_j(t) = 0 \tag{35}$$

By seeking the harmonic solutions under the forms:

$$q_j(t) = \tilde{q}_j(\omega) e^{\mathrm{i}\omega t}, \qquad V_i(t) = \tilde{V}_i(\omega) e^{\mathrm{i}\omega t}, \qquad F_j(t) = \tilde{F}_j(\omega) e^{\mathrm{i}\omega t}, \tag{36}$$

the final system of modal equations (Eqs. 37, 38) reads:

$$-\omega^2 \bar{m}\tilde{q}_j + \omega_j^2 \bar{m}\tilde{q}_j + \mathrm{i}\omega\eta_j \tilde{q}_j - \sum_{i=1}^{n_p} g_{ij}\tilde{V}_i = \tilde{F}_j, \quad (j = 1..N) \tag{37}$$

$$C_i \tilde{V}_i + \sum_{j=1}^{N} g_{ij}\tilde{q}_j = 0, \quad (i = 1..n_p) \tag{38}$$

2.4. Optimization of the transducers positions

In this section, an optimization procedure is described for positioning the piezoelectric patch on a structure so that the measurement of specific modes is maximized. The aim is to find the utility function that represents the piezoelectric patch sensitivity as a function of the specific modes of interest. More specifically, we intend to find the optimal placement a_i for the patch such as the coupling g_{ij} between the i-th patch and the j-th mode is maximized.

2.4.1. Modal sensitivity

We compute $\tilde{q}_j$ from Eq. (37), then inject the result into Eq. (38). By neglecting the quadratic terms with respect to the coupling term g_{ij}, we obtain the so called sensor equation for each patch i:

$$\tilde{V}_i = -\sum_{j=1}^{N} \frac{g_{ij}\tilde{F}_j}{C_i\bar{m}(\omega_j^2 - \omega^2 + \mathrm{i}\omega\eta_j/\bar{m})} \tag{39}$$

In our case the external force is a point force applied at a specific point of the beam x_f, with amplitude $\tilde{F}_0(\omega)$, i.e. $\tilde{p}(x,\omega) = F_0(\omega)\delta(x - x_f)$. This means that:

$$\tilde{F}_j = \int_0^\ell \tilde{p}(x,\omega)\phi_j(x)dx = \int_0^\ell \tilde{F}_0(\omega)\delta(x - x_f)\phi_j(x)dx = \tilde{F}_0\phi_j(x_f) \tag{40}$$

then the voltage measured on each piezo is:

$$\tilde{V}_i = -\sum_{j=1}^{N} g_{ij}\frac{\tilde{F}_0(\omega)\phi_j(x_f)}{C_i\bar{m}(\omega_j^2 - \omega^2 + \mathrm{i}\omega\eta_j/\bar{m})} \tag{41}$$

Finally, we can define the transfer function at the i-th patch as:

$$H_i(\omega) = \frac{\tilde{V}_i(\omega)}{\tilde{F}_0(\omega)} = -\sum_{j=1}^{N} \frac{g_{ij}\phi_j(x_f)}{C_i\bar{m}(\omega_j^2 - \omega^2 + \mathrm{i}\omega\eta_j/\bar{m})} \tag{42}$$

This transfer function is at the core of the optimization process.

The contribution of the j-th mode to the frequency response function Eq. (42) is:

$$G_{ij}(\omega) = \left| \frac{g_{ij}\phi_j(x_f)}{C_i\bar{m}(\omega_j^2 - \omega^2 + \mathrm{i}\omega\eta_j/\bar{m})} \right|$$

In order to estimate the sensitivity of each piezo patch i to mode j, with respect to the position a_i, we can introduce the following norm $\|.\|_\infty$, that in our case corresponds to evaluating the contribution of the j-th mode at resonance frequency ω_j:

$$\kappa_{ij} = \|G_{ij}(\omega_j)\|_\infty = \left| \frac{g_{ij}\phi_j(x_f)}{C_i\mathrm{i}\omega_j\eta_j} \right| \tag{43}$$

For each given patch i, a normalised form of modal sensitivity to mode j is given by:

$$\mathcal{M}_{ij} = \frac{\kappa_{ij}}{\max\limits_{j=1..N} \kappa_{ij}} \tag{44}$$

where $\mathcal{M}_{ij}$ represents the control authority of the i-th patch fixed over the j-th mode. Since the aim is to maximize the sensitivity of the piezoelectric sensor in regard to the detection of one or several mode(s) rather than using the patch as an actuator to control the mode(s), in this paper, it is named *modal sensitivity* in comparison with notion of *modal controllability* used in Halim and Moheimani [14].

2.4.2. Definition of a new utility function

Different utility functions can be defined starting from the concept of modal sensitivity. The idea is to obtain modal filtering, which is achieved by adding a weight in the optimization for specific modes. In this way it is possible to "see" or "hide" a mode [21]. To this end we define a vector $\boldsymbol{\xi}$ of modal weights, whose the component ξ_j corresponds to weight of the j-th mode:

$$\xi_j = \begin{cases} 1 \text{ if the } j\text{-th mode has to be seen} \\ -1 \text{ if the } j\text{-th mode has to be hidden} \\ 0 \text{ if the } j\text{-th mode is not relevant} \end{cases} \tag{45}$$

Then, for each value of a_i, b_i of the transducer and assuming that x_f is fixed, the utility function is defined as:

$$\mathcal{F}(a_i, b_i, x_f) = \sum_{j=1}^{N} \xi_j \mathcal{M}_{ij}(a_i, b_i, x_f) \tag{46}$$

and the optimal positions $\left\{\hat{a}_i, \hat{b}_i\right\}$ is defined by:

$$\left\{\hat{a}_i, \hat{b}_i\right\} = \arg\max(\mathcal{F}(a_i, b_i, x_f)) \tag{47}$$

Several transducers can be optimized at the same time, by choosing local maxima of the transfer function. In this case, constraints on transducers sizes have to be considered to avoid the overlap of two patches. The practical application of the method will be detailed in the case study presented in Section 3.

3. Case study : optimal transducers positioning for implant stability monitoring

The optimization method described in Section 2.4 is applied to a square beam named ancillary hereafter, and connected to an inaccessible mechanical system corresponding to an orthopedic implant into a bone mimicking phantom (Fig. 2). The ancillary is a part fixed to the implant during the surgery in order to

enable the surgeon to apply hammer impact at one of its extremity, leading to implant insertion. The aim of this case study is to present and validate a procedure of piezoelectric patches placement optimization for monitoring the stability of an implant which is not directly accessible for vibration measurement. The optimization principle lies on focusing on specific modes of vibration of the ancillary, which are sensitive to implant stability into the bone, and to hide modes which are not of biomechanical interest.

3.1. Geometry

A stainless steel beam of square section was designed with the geometrical and material properties given in Table C.4 (see Appendix C.1). The bottom threaded extremity was rigidly fixed in the implant and the top extremity was kept free. The implant was a cementless femoral stem made of titanium alloy (TiAl6Al4V) and coated with hydroxyapatite (CERAFIT RMIS, Ceraver, Roissy, France). The implant was fully inserted into a bone mimicking phantom (ORTHObones, 3B Scientific, Hamburg, Germany) embedded in polymer resin in order to enable clamping to the vibration table, similarly as what was done in [20, 32].

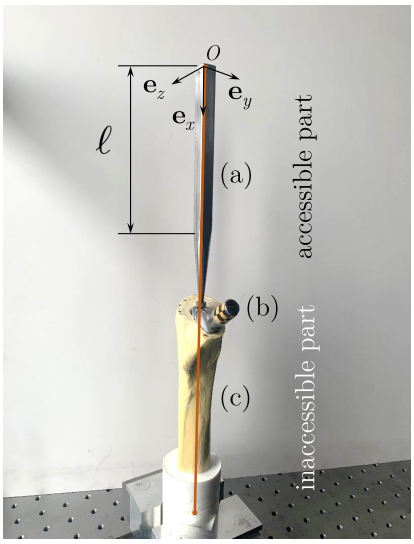

Figure 2: Experimental case study configuration. The same notations as the ones shown in Figure 1 are indicated : accessible instrumented length ℓ, axis directions and coordinates origin O. The ancillary (a) corresponds to the accessible part, the implant (femoral stem) (b) and the bone (femur) (c) represent the inaccessible part.

3.2. Optimization algorithm

The experimental optimization approach consists in the following successive steps described in Fig. 3:

1. **Modal characterization of the ancillary without piezoelectric sensors**. The modes of vibration of the ancillary are measured in the frequency range [0.4 12.8] kHz by Experimental Modal Analysis

(EMA). The experimental mode shapes ϕ_j^e, the resonance frequencies $f_j = 2\pi\omega_j$ and the damping coefficients $\beta_j = \eta_j/\bar{m}$ are retrieved.

2. **Piezoelectric patches placement optimization**. Different utility functions are defined from Eq. (46) based on the modal sensitivity $\mathcal{M}_{ij}$ calculated for each position a_i of piezo i and mode j. Considering the information carried by each mode j on the implant stability, a vector $\boldsymbol{\xi}$ is defined. For each utility function $\mathcal{F}$, the optimal piezoelectric patch position $\{\hat{a}_i, \hat{b}_i\}$ is determined by Eq. (47). One patch is associated with one utility function and n_p patches are used.

3. **Piezoelectric patches placement validation**: The amplitude ratios at ω_j are calculated between the frequency response functions H_i, measured successively with each piezoelectric patch i. The results are compared with what was expected from the definition of each utility function $\mathcal{F}$.

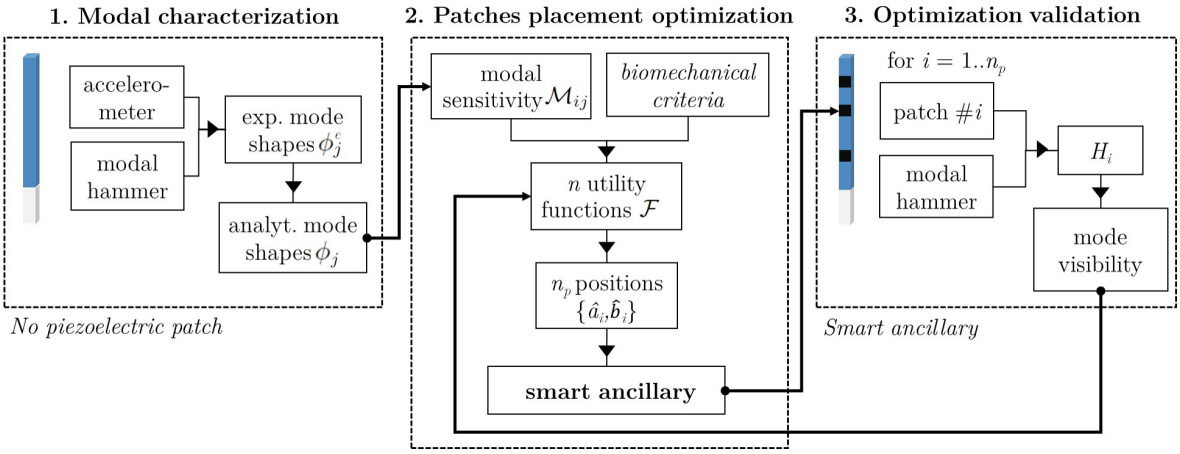

Figure 3: Experimental procedure for piezoelectric patches placement optimization and protocol validation.

3.3. Modal characterization of the ancillary

Modal analysis measurements. The ancillary modal features were determined by performing EMA following the same protocol described in [20] and shown in Fig. 4. Only the mode shapes oscillating along $\boldsymbol{e}_z$, were measured, since the properties of the mode shapes along $\boldsymbol{e}_y$ were shown to not evolve with implant insertion into the bone in a previous study [20]. The structure was excited by hammer impacts (modal hammer 8204, *Brüel & Kjaer, Naerum, Denmark*) at 13 locations x_f equally spaced of 10 mm beginning at 5 mm from the ancillary top surface. At each location, the structure was excited 5 times along $\boldsymbol{e}_z$ (see Fig. 4). The z-accelerations consecutive to each impact were recorded by a tri-axial accelerometer (365A01PCB *Piezotronics, Depew, NY, USA*) glued at the ancillary top extremity, as shown in Fig. 4. The excitation impact was lower than 50N to ensure it does not modify the implant position and consequently the boundary

conditions of the beam during the modal features measurement. A dedicated data acquisition module (BK Connect, *Brüel & Kjaer, Naerum, Denmark*) with a sampling rate of 51.2 kHz was used to record the acceleration signals during 0.25 s. We assume that the weight of the accelerometer (1 g) and the weight and rigidity of the piezoelectric patches do not influence the structure dynamic behavior.

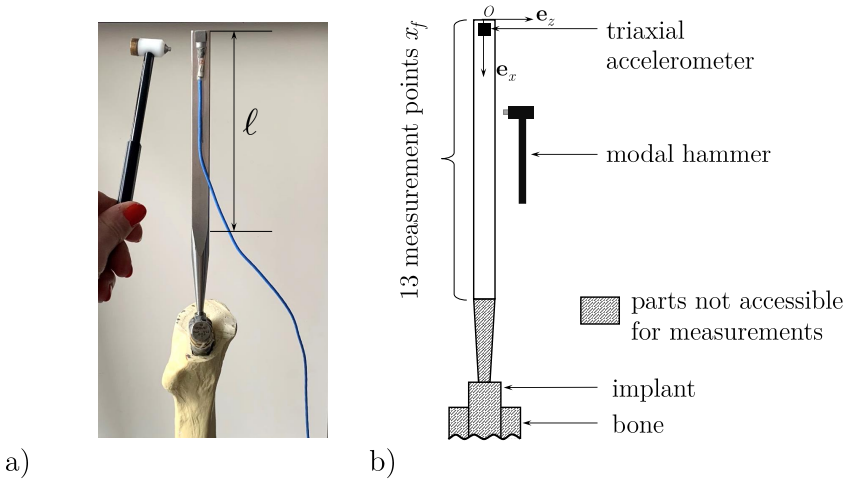

Figure 4: a) Picture and b) scheme of the Experimental Modal Analysis set-up with ℓ =125 mm.

Modes selection. An example of two frequency response functions (*frf*) measured in the range [0.4 12.8] kHz for an impact at $x_f = 5$ mm along $\boldsymbol{e}_z$, is presented in Fig. 5. The two *frf* correspond to two different implant insertion stages, one at beginning of insertion (in grey) and one for the implant fully seated (in black). The choice to show *frf* corresponding to an impact location at $x_f = 5$ mm is explained because it is a good compromise to see all the modes on the frequency range [0.4 12.8] kHz, due to the proximity to the free extremity, where the mode shapes are close.

Five modes were selected from the *frf* of implant fully inserted, for the patch placement optimization analysis, denoted A, B, C, D and E hereafter. Table 1 gathers the modal features of the five selected modes obtained for the implant fully seated : resonance frequency f and damping factor β, calculated for each resonance frequency with the 3 dB method. The resonance frequencies of modes A and B are in good agreement with what was found in [20]. These two resonance frequencies increase during implant insertion into the bone and reach values of 2.6 kHz and 3.3 kHz once the implant fully seated, which corresponds to the behavior of modes $2Y$ and $2Y_b$, identified in [20].

Mode shapes. The experimental modal shapes ϕ_j^e of the five selected modes presented in Table 1 and in Fig. 5 are shown in Fig. 6. The five modes are of bending nature, with either two nodes (modes A, B and C) are

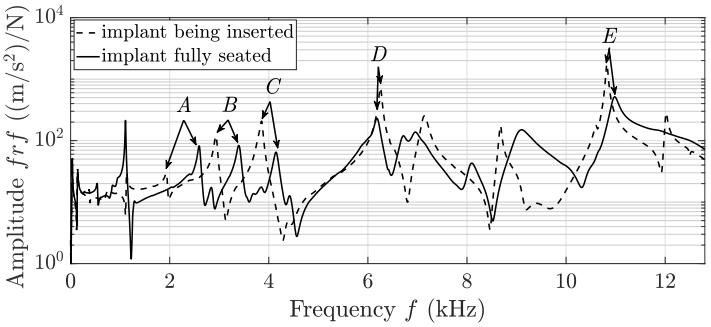

Figure 5: Frequency response functions, *frf*, measured by the accelerometer for an impact at $x_f = 5$ mm along $\boldsymbol{e}_z$ at beginning (in grey) and end (in black) of implant insertion. The letters from A to E indicate the modes selected for the patch placement optimization analysis.

Mode #	***A***	***B***	***C***	***D***	***E***
f (Hz)	2609	3391	4160	6157	10956
β (-)	2.19	1.20	1.74	1.86	0.64

Table 1: Names and modal features (resonance frequency f, damping factor β) of the modes selected for the piezoelectric patches placement optimization procedure.

three nodes for higher resonance frequencies (modes D and E). This result confirms that mode A and B correspond to modes $2Y$ and $2Y_b$ in [20]. Each mode shape ϕ_j^e was normalized by its Euclidean norm $||.||_2$. Each discrete experimental mode shape ϕ_j^e, was fitted using the general equation of normal beam shapes adapted from Eq. (31):

$$\phi_j^{(4)} = \frac{\omega_j^2 \bar{m}}{\mathcal{D}} \phi_j \tag{48}$$

where $\lambda_j^{(4)} = \omega_j^2 \bar{m}/\mathcal{D}$. Hence, the general solution of Eq. (48) is given by:

$$\phi_j = C_1 \sin(\lambda_j x) + C_2 \cos(\lambda_j x) + C_3 \sinh(\lambda_j x) + C_4 \cosh(\lambda_j x) \tag{49}$$

where the constant $C_{1,2,3,4}$ are determined from the boundary conditions expressed by Eq. (26) to (29). In our case study, considering a free end at $x = 0$, the bending moment and shear force were both equal to zero at this end (Eq. (26) and Eq. (27)) which gives $C_1 = C_3$ and $C_2 = C_4$. Then, for each mode j, the values of C_1 and C_2 were determined using an error minimization algorithm in Matlab. The mode shapes were fitted in order to further calculate the coupling coefficient g_{ij} from the mode shape curvature $\phi_j{}''$ (Eq. 34), which requires a continuous shape.

3.4. Piezoelectric patches placement optimization

This section is dedicated to the definition of one or more utility function(s) $\mathcal{F}$ aiming at finding patches positions $\hat{a}_i$ $(i = 1..n_p)$ on the ancillary such as a combination of modes ϕ_j $(j = 1..N)$ are visible or hidden

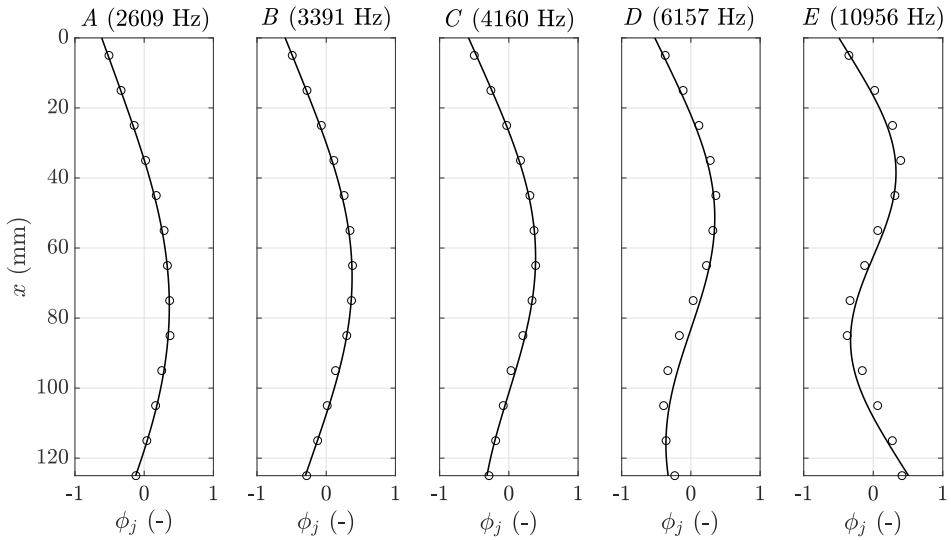

Figure 6: Experimental (o) and fitted (-) mode shapes ϕ_j of modes A to E, vibrating along $\boldsymbol{e}_z$.

when measuring the frequency response function H_i by the piezoelectric patch i. The choice to see or hide one or several mode(s) is based on the mode resonance frequency sensitivity to the implant position into the bone, corresponding to the so-called "inaccessible part". The modes ϕ_j considered for the optimization analysis are modes $\#A$, B, C, D and E.

Piezoelectric patch properties. The piezoelectric transducers that are used for resonance frequency functions measurement are square shaped with a length $b = h = 10$ mm and a thickness $h_p = 0.2$ mm. The geometry is fixed and constant over the patches. The detailed properties or given in Table C.5 in the Appendix C.2. The same configuration as presented in Section 2.1 and Fig. 1 with two piezoelectric patches put symmetrically at the upper and lower surfaces of the beam is considered hereafter.

Modal sensitivity. As described in Section 2.4, the normalized modal sensitivity $\mathcal{M}_{ij}$ defined by Eq. (44) is calculated for each mode j and patch i by varying the position a_i of the patch. As the length ℓ of the instrumented beam is 125 mm and the patches are 10 mm length, $a_i \in$ [0-115] mm, in order to avoid the patch to exceed the accessible part of the structure. The spatial resolution for varying the position a_i of the patch and calculating $\mathcal{M}_{ij}$ is 1 mm.

For each mode j, the results show at least one minimum and maximum on the modal sensitivity function $\mathcal{M}_{ij}$ (see Fig. 7) depending on the patch position a_i. The higher frequency modes D and E (6157 Hz and 10956 Hz, respectively) have two local maxima which offer two possibilities for patch placement whereas lower frequency modes A, B and C (2609 Hz, 3391 Hz and 4160 Hz, respectively) only hold one maximum.

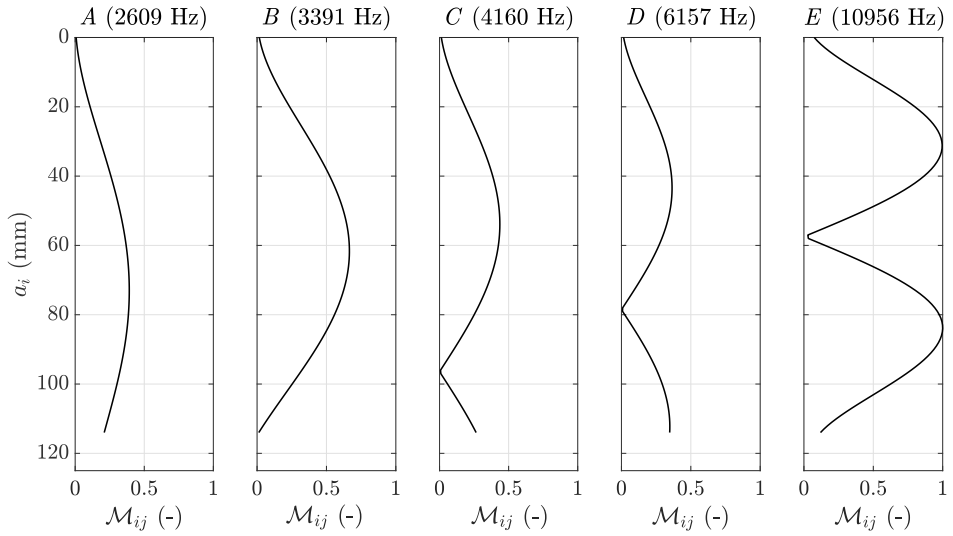

Figure 7: Modal sensitivities $\mathcal{M}_{ij}$ depending on the patch position a_i on the ancillary calculated for each mode A to E.

Choice of transducers positions. The strategy employed for the definition of a utility function $\mathcal{F}$ is to use one transducer associated to multiple modes, as explained in the section 2.4.2. Different utility functions can be defined, each function being associated with an optimal patch position $\{\hat{a}_i, \hat{b}_i\}$, defined by Eq. (47). The comparison of the *frf* measured at the beginning of implant insertion and once the implant is fully seated (see Fig. 5) shows that 4 modes (namely, modes #A, B, C and E) over the 5 selected for the study, are sensitive to implant stability with a frequency shift of more than 150 Hz to higher frequencies between the beginning and end of implant insertion. The sensitivity of the modes A and B is in good agreement with what was obtained in [20].

From these results and in order to demonstrate the performance of the optimization method, three examples of utility functions $\mathcal{F}$ are defined with Eq. (46), for which the modal weights ξ_j associated to each mode j are shown in Table 2. Considering these examples, each utility function $\mathcal{F}$ is associated with one position $\hat{a}_i$ of the patch i such as:

- $\mathcal{F}_1$: The resulting position $\hat{a}_1$ of the patch assumes to be the best compromise to see all the modes A to E on the frequency response function (ξ_j=1). This configuration acts as a *reference case*, which will allow the comparison with other configurations where modes should be filtered ($\mathcal{F}_2$, $\mathcal{F}_3$), in order to evaluate the efficiency of the optimization method.

- $\mathcal{F}_2$: The resulting position $\hat{a}_2$ of the patch assumes to be the best compromise to hide mode D (ξ_4=-1) while letting the other modes visible ($\xi_{j\neq4}$=1). This configuration enables to focus only on the modes

sensitive to implant insertion (namely, modes A, B, C and E), since the resonance frequency of mode D has shown to not significantly change during implant insertion (see Fig. 5).

- $\mathcal{F}_3$: The resulting position $\hat{a}_3$ of the patch assumes to be the best compromise to filter mode C (ξ_3=-1) while ensuring visibility of mode B (ξ_2=1). The other modes are not concerned by the optimization configuration ($\xi_{1,4,5}$=0). This configuration enables to focus on the tracking of the resonance frequency of mode B for implant insertion monitoring, by avoiding confusing with mode C, due to their close resonance frequencies.

Modes	***A***	***B***	***C***	***D***	***E***	**$\{\hat{a}_i, \hat{b}_i\}$ (mm)**
$\boldsymbol{\mathcal{F}_1}$	**1**	**1**	**1**	**1**	**1**	**{40, 50}**
$\mathcal{F}_2$	1	1	1	-1	1	{78, 88}
$\mathcal{F}_3$	1	1	-1	1	1	{91, 101}

Table 2: Modal weights ξ_j defined for the utility functions $\mathcal{F}_{1,2,3}$ and resulting optimal piezoelectric positions $\hat{a}_1$, $\hat{a}_2$, $\hat{a}_3$. The reference case corresponding to $\mathcal{F}_1$ is highlighted in bold.

Figure 8b shows the three utility functions $\mathcal{F}_1$, $\mathcal{F}_2$, $\mathcal{F}_3$ calculated for the weight coefficients ξ_j defined in Table 2. The modal sensitivities $\mathcal{M}_{ij}$ are represented in Fig. 8a for $j = 1..5$. For each utility function, only one maximum is identified, corresponding to the position $\hat{a}_i$ of the piezoelectric patch defined by Eq. (47). Note that to avoid overlap, for each patch i, we verified that $|\hat{a}_i - \hat{a}_{i+1}| > b$, in order to allow the bounding of the 3 transducers on the same beam.

3.5. Validation of optimization placement protocol

The structure has been assembled following the optimization procedure described in the previous section. The piezoelectric patches have been bonded on the surface of the beam using a one-component silver-filled epoxy resin (Elecolit 3043, *Panacol, Germany*) cured at 160°C during 30 min. The resulting smart ancillary is shown in Fig. 9.

To assess the validity of the patches placement optimization procedure, a frequency analysis was performed in order to compare the frequency response functions H_i measured by each patch i. To do so, the ancillary was excited by a modal hammer, impacting the structure at $x_f = 5$ mm along $\boldsymbol{e}_z$. The choice of the position of the source x_f is explained by the similarity of the mode shapes near the free extremity (see Fig. 6), which provides optimization results independent of x_f. However, as shown in Eq. (42), it would have been possible to study and optimize the position of the excitation source x_f in the calculation of the utility functions $\mathcal{F}$. The system dynamic response was measured successively by one of the three piezoelectric patches, the two others being short-cut during the acquisition time. The sampling frequency

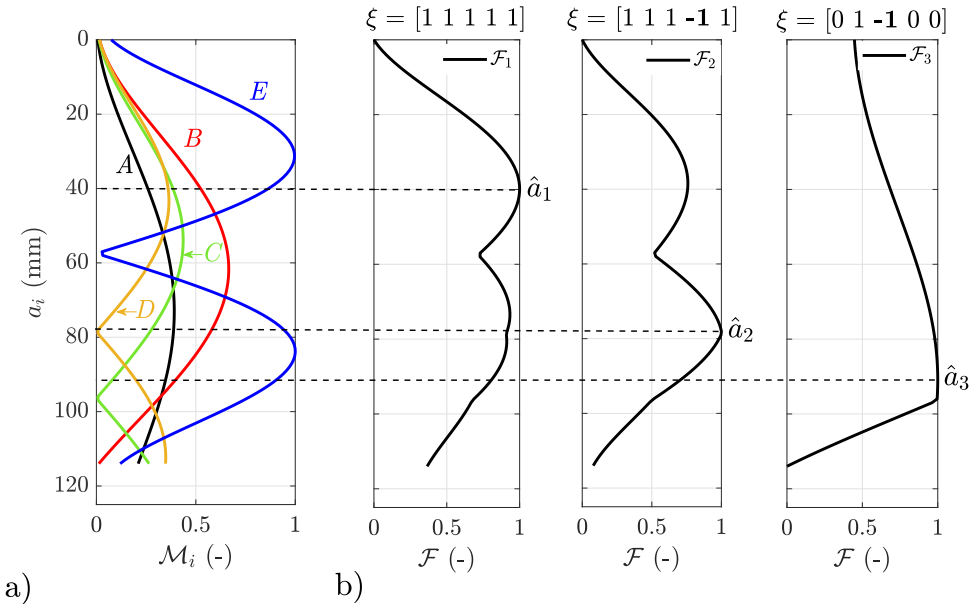

Figure 8: a) Modal sensitivities $\mathcal{M}_{ij}$ as a function of the patch position a_i calculated for $j = 1..5$ (namely, modes A to E) and b) corresponding utility functions $\mathcal{F}_{1,2,3}$ calculated for $\boldsymbol{\xi}$ =[1 1 1 1 1], $\boldsymbol{\xi}$ =[1 1 1 -1 1] and $\boldsymbol{\xi}$ =[0 1 -1 0 0], respectively, with the optimal positions $\hat{a}_i$ corresponding to the maximum of each utility function $\mathcal{F}$.

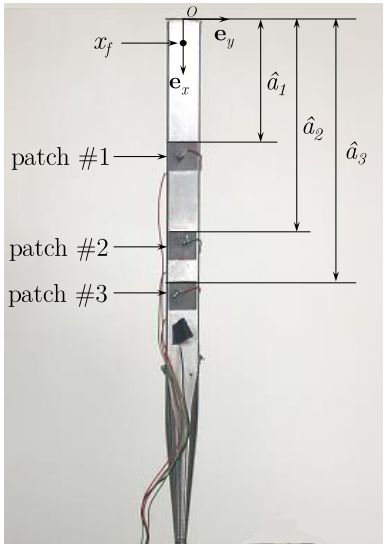

Figure 9: Image of the instrumented ancillary equipped with piezoelectric patches #1, #2, #3 bonded at locations $\hat{a}_1 = 40$ mm, $\hat{a}_2 = 78$ mm and $\hat{a}_3 = 91$ mm, calculated from the optimization procedure described in Section 3.4

and the acquisition time were the same as for the modal characterization, leading to a frequency resolution $df = 4$ Hz.

The frequency response function H_1 obtained by the piezoelectric patch #1, placed such as the utility function allow the visibility of all the set of modes A to E, is compared with H_2 measured by the piezoelectric

patch #2 in Fig. 10a and with H_2 measured by the piezoelectric patch #3 in Fig. 10b. The amplitudes at resonances measured by the three piezoelectric patches are given in Table 3 together with the amplitude's variation at resonance obtained for patch #2 and patch #3 with respect to the reference patch #1.

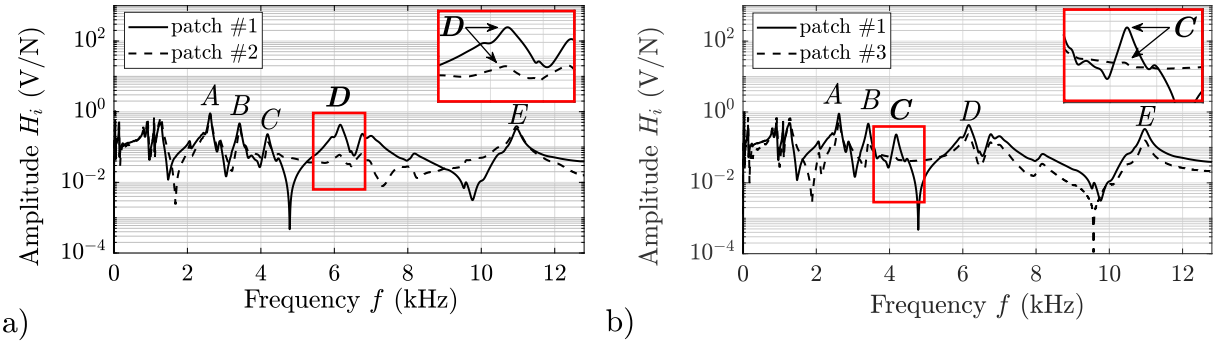

Figure 10: a) Comparison of the frequency response functions H_1 and H_2 measured by the piezoelectric patch #1 and the piezoelectric patch #2 and b) comparison of H_1 and H_3 measured by the piezoelectric patch #1 and the piezoelectric patch #3. A zoom on the target modes by the utility functions $\mathcal{F}_2$ and $\mathcal{F}_3$ is included in the graphs.

Modes	***A***	***B***	***C***	***D***	***E***
patch #1 (V/N)	**0.898**	**0.467**	**0.231**	**0.427**	**0.330**
patch #2 (V/N)	0.851 (-5.24%)	0.337 (-27.8%)	0.136 (-41.3%)	0.060 (-85.9%)	0.386 (+17.0%)
patch #3 (V/N)	0.600 (-33.2%)	0.152 (-67.4%)	0.054 (-76.8%)	0.234 (-45.2%)	0.156 (-52.7%)

Table 3: Amplitudes at resonances of modes A to E measured by patches #1, #2, #3 together with the percentage of amplitude's decrease at resonance indicated in brackets, with regard to measurements from patch #1. The patch #1 corresponds to the reference case and is highlighted in bold.

The amplitude decrease of 85.9% of mode D measured by the piezoelectric patch #2 with regard to patch #1, validates the position optimization procedure since the utility function $\mathcal{F}_2$ aimed to hide mode D. Similarly, the frequency measurement with the patch #3 leads to a decrease of 76.9% of the amplitude of the mode C with regard to patch #1, which was expected by the utility function $\mathcal{F}_3$. Nevertheless, the unintended associated decrease of the amplitude of mode B show the limitation of the utility function, defined by weight coefficient ξ_j and patch position a_i. This unintended decrease is explained by the strong similarity between the shapes of mode B and C (see Fig. 6). Therefore, another condition based on a minimum visibility of the modes associated with ξ_j=1 should be implemented in the utility function to ensure mode visibility. It could also be relevant to study the effect of the geometrical parameters of the piezoelectric patch as the length b or the thickness h_p, both implied in the calculation of the coupling coefficient g_{ij} and therefore $\mathcal{M}_{ij}$.

4. Conclusion and discussions

This paper proposes a method for optimizing the positioning of piezoelectric patches on a beam attached to an unreachable structure. The issue of maximizing the observability on the frequency response function of a set of modes, which is sensitive to the beam boundary conditions, was addressed. For that purpose, an optimization strategy was developed, based on the definition of utility functions, expressed in terms of modal weight and in terms of the so-called modal observability, for which the expression has been exhibited. It has been shown that the modal observability depends on the electro-mechanical coupling coefficient, calculated from the patches geometrical and material properties, and the beam mode shapes curvatures. The originality of the paper comes from the use of the modal electro-mechanical coupling factor (MEMCF) to optimize sensors placement on the beam in order to improve beam boundary condition monitoring. An original application for implant stability measurement was proposed.

In the particular case developed in this paper, one piezoelectric patch is associated to several modes, whose the observability has to be improved. Therefore, the optimal piezoelectric patches positions are the result of a compromise obtained from the utility functions, aiming at improving the observability of a set of modes sensitive to beam boundary conditions, while minimizing the observability of the modes which are not sensitive to them. In the experimental case study, the particular issue of monitoring implant stability by means of a smart beam was investigated. The smart beam, which is basically a tool used by the surgeon to insert the implant, was equipped with patches for which the placement was determined to optimize the mode observability on the FRF, depending on the sensitivity to the stability, that was demonstrated in a previous study [20]. The mode observability measured by the position-optimized patches was in good agreement with what was expected from the utility functions definition. The amplitude of the modes that should be hidden on the FRF because they are not sensitive to implant stability decreased up to 85% with regard to the reference position. The results of this study open the path towards the conception of a smart tool optimized for the real-time monitoring of implant stability during the insertion of an implant by the surgeon.

However, since the optimization strategy is based on the modal observability and in particular the coupling coefficient, the positions strongly depend on the mode shapes curvatures. For low frequency modes, the placement possibilities are limited because of the few number of nodes, and therefore close mode shapes will tend for close piezoelectric patches positions. Moreover, another drawback of the study is that optimization of the dimensions of the piezoelectric patches was not studied, whereas the electro-mechanical coefficient also depends on the thickness or the length of the patch. This aspect was studied in [11] and

could be easily implemented in the strategy proposed in this paper. Another way of optimization, would be to use specific forms of piezoelectric patches, enabling accurate boundary force measurement, as proposed in [33]. Nevertheless, this method is more complex to implement regarding both the piezoelectric patch design and the post-processing analysis.

The method proposed in this paper is particularly adapted for applications where mode shapes change with boundary conditions, as it relies on mode shape curvatures. It could be applied for other configurations of beam-like structures with bending modes that should be tuned, based on the modal observability concept. Also, a relevant perspective will be to investigate the placement optimization of the excitation source, and in particular, by using one of the piezoelectric patch as an actuator. This outlook is of particular interest concerning the biomedical application presented in the case study, since it would lead to an automation of the measurement by preventing from the use of a modal hammer as a source of excitation that is not convenient in a clinical environment. Then, as investigated by several authors [23, 24, 6], another strategy approach could be to use of a network of sensors along the beam with different control signals to tune specific modes. The main advantage of this approach would be to conceive one unique beam for several applications.

5. Acknowledgments

This project has received funding from the European Research Council (ERC) under the European Union's Horizon 2020 research and innovation program (grant agreement No 682001, project ERC Consolidator Grant 2015 BoneImplant), from the project OrthAncil (ANR-21-CE19-0035-03) and from the project OrthoMat (ANR-21-CE17-0004).

Appendix A. Constitutive equations of piezoelectric materials

Constitutive equations. Assuming a linear piezoelectric material, the 3D constitutive equations may be written in matrix form as follows [34]:

$$\begin{pmatrix} \boldsymbol{\sigma} \\ \boldsymbol{D} \end{pmatrix} = \begin{bmatrix} \mathbf{c} & -\mathbf{e}^T \\ \mathbf{e} & \boldsymbol{\varepsilon} \end{bmatrix} \begin{pmatrix} \boldsymbol{\epsilon} \\ \boldsymbol{E} \end{pmatrix} \tag{A.1}$$

where $\boldsymbol{\sigma} = (\sigma_{xx}, \sigma_{yy}, \sigma_{zz}, \sigma_{yz}, \sigma_{xz}, \sigma_{xy})^T$ is the stress vector; $\boldsymbol{D} = (D_x, D_y, D_z)^T$ is the electric displacement vector; $\boldsymbol{\epsilon} = (\epsilon_{xx}, \epsilon_{yy}, \epsilon_{zz}, 2\epsilon_{yz}, 2\epsilon_{xz}, 2\epsilon_{xy})^T$ is the strain vector; and $\boldsymbol{E} = (E_x, E_y, E_z)^T$ is the electric field vector. The matrices $\mathbf{c}$, $\mathbf{e}$, $\boldsymbol{\varepsilon}$ are the matrices with elastic, electro-mechanic and dielectric constant entries.

$$\mathbf{c} = \begin{bmatrix} c_{11} & c_{12} & c_{13} & 0 & 0 & 0 \\ c_{21} & c_{22} & c_{23} & 0 & 0 & 0 \\ c_{31} & c_{32} & c_{33} & 0 & 0 & 0 \\ 0 & 0 & 0 & c_{44} & 0 & 0 \\ 0 & 0 & 0 & 0 & c_{55} & 0 \\ 0 & 0 & 0 & 0 & 0 & c_{66} \end{bmatrix}, \mathbf{e} = \begin{bmatrix} 0 & 0 & 0 & 0 & e_{15} & 0 \\ 0 & 0 & 0 & e_{24} & 0 & 0 \\ e_{31} & e_{32} & e_{33} & 0 & 0 & 0 \end{bmatrix}, \boldsymbol{\varepsilon} = \begin{bmatrix} \varepsilon_{11} & 0 & 0 \\ 0 & \varepsilon_{22} & 0 \\ 0 & 0 & \varepsilon_{33} \end{bmatrix}, \tag{A.2}$$

Alternatively, the equation (A.1) may be written by:

$$\begin{pmatrix} \boldsymbol{\epsilon} \\ \boldsymbol{D} \end{pmatrix} = \begin{bmatrix} \mathbf{s} & \mathbf{d} \\ \mathbf{d}^T & \boldsymbol{\varepsilon} \end{bmatrix} \begin{pmatrix} \boldsymbol{\sigma} \\ \boldsymbol{E} \end{pmatrix} \tag{A.3}$$

where $\mathbf{s} := \mathbf{c}^{-1}$ is the compliance matrix and $\mathbf{d} := \mathbf{s}\mathbf{e}^T$ contains the piezoelectric constants. Note that $Y_b = 1/s_{11}$.

Appendix B. Extended Hamilton principle

Energy density function. The total stored energy density in a unit volume of material is the sum of the mechanical work and of the electrical work [31]:

$$dW_e(\boldsymbol{\epsilon}, \boldsymbol{D}) = (d\boldsymbol{\epsilon})^T \boldsymbol{\sigma} + (d\boldsymbol{D})^T \boldsymbol{E} \tag{B.1}$$

Note that for a conservative system, $W_e = \int_{(0,0)}^{(\epsilon, D)} dW_e$ which leads to the constitutive equation:

$$\boldsymbol{\sigma} = \frac{\partial W_e}{\partial \boldsymbol{\epsilon}}, \quad \text{and} \quad \boldsymbol{E} = \frac{\partial W_e}{\partial \boldsymbol{D}} \tag{B.2}$$

The coenergy density function is defined by:

$$W_e^*(\boldsymbol{\epsilon}, \boldsymbol{E}) = \boldsymbol{E}^T \boldsymbol{D} - W_e(\boldsymbol{\epsilon}, \boldsymbol{D}) \tag{B.3}$$

By calculating the total differential of dW_e^* and by using the (A.1), we can express W_e^* as:

$$W_e^*(\boldsymbol{\epsilon}, \boldsymbol{E}) = \frac{1}{2}\boldsymbol{E}^T \boldsymbol{\varepsilon} \boldsymbol{E} + \boldsymbol{\epsilon}^T \mathbf{e} \boldsymbol{E} - \frac{1}{2}\boldsymbol{\epsilon}^T \mathbf{c} \boldsymbol{\epsilon} \tag{B.4}$$

It follows that:

$$\boldsymbol{\epsilon} = \frac{\partial W_e^*}{\partial \sigma}, \quad \text{and} \quad \boldsymbol{S} = \frac{\partial W_e^*}{\partial \boldsymbol{E}} \tag{B.5}$$

Hamilton's principle. We assume the admissibility requirements which impose that the virtual displacements $\delta \boldsymbol{u}$ must be compatible with the the kinematic of the system, and the admissible flux linkage variation $\delta\lambda$ must be compatible with Kirchhoff's voltage rule. The Hamilton's principle reads [2]:

$$\int_{t_1}^{t_2} (\delta T^* + \delta W_e^* + \delta W_{ext}) = 0 \tag{B.6}$$

where

$$T^* = \frac{1}{2}\int_\Omega \rho \dot{\boldsymbol{u}}^T \dot{\boldsymbol{u}}\, dV \tag{B.7}$$

$$W_e^* = \frac{1}{2}\int_\Omega \left(\boldsymbol{E}^T \boldsymbol{\varepsilon} \boldsymbol{E} + 2\boldsymbol{\epsilon}^T \mathbf{e} \boldsymbol{E} - \boldsymbol{\epsilon}^T \mathbf{c} \boldsymbol{\epsilon} \right) dV \tag{B.8}$$

and which follows that:

$$\delta T^* = \int_\Omega \rho \delta \dot{\boldsymbol{u}}^T \dot{\boldsymbol{u}}\, dV \tag{B.9}$$

$$\delta W_e^* = \int_\Omega \left(\delta \boldsymbol{E}^T \boldsymbol{D} - \delta \boldsymbol{\epsilon}^T \boldsymbol{\sigma} \right) dV \tag{B.10}$$

The term δW_{ext} represents the virtual work of the external forces and of the external applied currents:

$$\delta W_{ext} = \int_\Omega \delta \boldsymbol{u}^T \boldsymbol{f}_v dV + \int_{S_f} \delta \boldsymbol{u}^T \boldsymbol{f}_s dS - \int_{S_q} \delta \phi^T \bar{q} dS, \tag{B.11}$$

where $\boldsymbol{f}_v$ is the volume force, $\boldsymbol{f}_s$ is the surface forces applied on S_f, $\bar{q}$ is surface charge density applied on S_q.

Appendix C. Properties of the ancillary and the piezoeletric patches

Appendix C.1. Ancillary

Properties of the ancillary		
Coefficient	Value	Description
A	10×10 mm^2	Section of the ancillary
h	10 mm	Thickness
ℓ	125 mm	Length of the ancillary (squared part only)
Y_b	193 GPa	Young's modulus
ρ	8000 kg m^{-3}	Density
μ	0.3	Poisson's ratio

Table C.4: Dimensions and mechanical properties of the ancillary

382 *Appendix C.2. Piezoelectric patches*

Properties of the piezoelectric ceramic		
Coefficient	Value	Description
h_p	0.2 mm	Thickness
b	10 mm	Length
d_{31}	-180×10^{-12} C/N	Coupling coefficient
Y_p	62.3 GPa	In-plane Young's Modulus
ρ_p	7800 kg m^{-3}	Density
μ_p	0.35	Poisson's ratio

Table C.5: Dimensions and mechanical properties of the piezoelectric ceramic element

References

[1] N. W. Hagood, A. von Flotow, Damping of structural vibrations with piezoelectric materials and passive electrical networks, Journal of Sound and Vibration 146 (2) (1991) 243–268. doi:10.1016/0022-460X(91)90762-9.

[2] M. Porfiri, C. Maurini, J. Pouget, Identification of electromechanical modal parameters of linear piezoelectric structures, Smart Materials and Structures 16 (2007) 323–331. doi:10.1088/0964-1726/16/2/010.

[3] O. Thomas, J. Ducarne, J.-F. Deü, Performance of piezoelectric shunts for vibration reduction, Smart Materials and Structures 21 (1) (2012) 015008. doi:10.1088/0964-1726/21/1/015008.

[4] C. H. Park, Dynamics modelling of beams with shunted piezoelectric elements, Journal of Sound and Vibration 268 (1) (2003) 115–129. doi:10.1016/S0022-460X(02)01491-8.

[5] U. Andreaus, F. Dell'Isola, M. Porfiri, Piezoelectric Passive Distributed Controllers for Beam Flexural Vibrations, Journal of Vibration and Control (2004) 625–657doi:10.1177/1077546304038224.

[6] F. Dell'Isola, C. Maurini, M. Porfiri, Passive damping of beam vibrations through distributed electric networks and piezoelectric transducers: prototype design and experimental validation, Smart Materials and Structures (2004) 299–308doi:10.1088/0964-1726/13/2/008.

[7] S. Vidoli, F. dell'Isola, Vibration control in plates by uniformly distributed PZT actuators interconnected via electric networks, European Journal of Mechanics - A/Solids 20 (3) (2001) 435–456. doi:10.1016/S0997-7538(01)01144-5.

[8] S. Alessandroni, U. Andreaus, F. Dell'Isola, M. Porfiri, A passive electric controller for multimodal vibrations of thin plates, Computers and Structures (2005) 15doi:10.1016/j.compstruc.2004.08.028.

[9] G. Rosi, J. Pouget, F. dell'Isola, Control of sound radiation and transmission by a piezoelectric plate with an optimized resistive electrode, European Journal of Mechanics - A/Solids 29 (5) (2010) 859–870. doi:10.1016/j.euromechsol.2010.02.014.

[10] V. Gupta, M. Sharma, N. Thakur, Optimization Criteria for Optimal Placement of Piezoelectric Sensors and Actuators on a Smart Structure: A Technical Review, Journal of Intelligent Material Systems and Structures 21 (12) (2010) 1227–1243. doi:10.1177/1045389X10381659.

[11] J. Ducarne, O. Thomas, J. F. Deü, Placement and dimension optimization of shunted piezoelectric patches for vibration reduction, Journal of Sound and Vibration 331 (14) (2012) 3286–3303. doi:10.1016/j.jsv.2012.03.002.

[12] I. Bruant, L. Gallimard, S. Nikoukar, Optimal piezoelectric actuator and sensor location for active vibration control, using genetic algorithm, Journal of Sound and Vibration 329 (10) (2010) 1615–1635. doi:10.1016/j.jsv.2009.12.001.

[13] M. Biglar, M. Gromada, F. Stachowicz, T. Trzepieciński, Optimal configuration of piezoelectric sensors and actuators for active vibration control of a plate using a genetic algorithm, Acta Mechanica 226 (2015) 3451–3462. doi:10.1007/s00707-015-1388-1.

[14] D. Halim, S. O. Reza Moheimani, An optimization approach to optimal placement of collocated piezoelectric actuators and sensors on a thin plate, Mechatronics 13 (1) (2003) 27–47. doi:10.1016/S0957-4158(01)00079-4.

[15] G. Qi, W. P. Mouchon, T. E. Tan, How much can a vibrational diagnostic tool reveal in total hip arthroplasty loosening?, Clinical Biomechanics 18 (5) (2003) 444–458. doi:10.1016/s0268-0033(03)00051-2.

[16] P. Henys, L. Capek, J. Fencl, E. Prochazka, Evaluation of acetabular cup initial fixation by using resonance frequency principle, Proceedings of the Institution of Mechanical Engineers, Part H: Journal of Engineering in Medicine 229 (1) (2015) 3–8. doi:10.1177/0954411914561485.

[17] K. Denis, L. C. Pastrav, S. Leuridan, Vibration Analysis of the Biomechanical Stability of Total Hip Replacements, in: Experimental Methods in Orthopaedic Biomechanics, Elsevier, 2017, pp. 313–328.

[18] S. A. Yousefsani, H. Dejnabadi, O. Guyen, K. Aminian, A Vibrational Technique for In Vitro Intraoperative Prosthesis Fixation Monitoring, IEEE transactions on bio-medical engineering 67 (10) (2020) 2953–2964. doi:10.1109/TBME.2020.2974380.

[19] S. Leuridan, Q. Goossens, L. C. Pastrav, M. Mulier, W. Desmet, J. Vander Sloten, K. Denis, Development of an Instrument to Assess the Stability of Cementless Femoral Implants Using Vibration Analysis During Total Hip Arthroplasty, IEEE Journal of Translational Engineering in Health and Medicine 9 (2021) 1–10. doi:10.1109/JTEHM.2021.3128276.

[20] A.-S. Poudrel, G. Rosi, V.-H. Nguyen, G. Haiat, Modal Analysis of the Ancillary During Femoral Stem Insertion: A Study on Bone Mimicking Phantoms, Annals of Biomedical Engineering 50 (1) (2022) 16–28. doi:10.1007/s10439-021-02887-9.

[21] G. Rosi, R. Paccapeli, F. Ollivier, J. Pouget, Optimization of piezoelectric patch positioning for passive sound radiation control of plates, Journal of Vibration and Control 19 (5) (2012) 658 – 673. doi:10.1177/1077546312437236.

[22] E. B. Flynn, M. D. Todd, Optimal Placement of Piezoelectric Actuators and Sensors for Detecting Damage in Plate Structures, Journal of Intelligent Material Systems and Structures 21 (3) (2010) 265–274. doi:10.1177/1045389X09338080.

[23] S. Zhao, N. Wu, Q. Wang, Crack identification through scan-tuning of vibration characteristics using piezoelectric materials, Smart Materials and Structures 26 (2) (2016) 025005. doi:10.1088/1361-665X/aa520a.

[24] S. Zhao, N. Wu, Q. Wang, Damage Detection of Beams by a Vibration Characteristic Tuning Technique Through an Optimal Design of Piezoelectric Layers, International Journal of Structural Stability and Dynamics 16 (10) (2016) 1550070. doi:10.1142/S0219455415500704.

[25] A. M. Sadri, J. R. Wright, R. J. Wynne, Modelling and optimal placement of piezoelectric actuators in isotropic plates using genetic algorithms, Smart Materials and Structures 8 (4) (1999) 490. doi:10.1088/0964-1726/8/4/306.

[26] A. R. Mehrabian, A. Yousefi-Koma, A novel technique for optimal placement of piezoelectric actuators on smart structures, Journal of the Franklin Institute 348 (1) (2011) 12–23. doi:10.1016/j.jfranklin.2009.02.006.

[27] I. Bruant, L. Gallimard, S. Nikoukar, Optimization of Piezoelectric Sensors Location and Number Using a Genetic Algorithm, Mechanics of Advanced Materials and Structures 18 (7) (2011) 469–475. doi:10.1080/15376494.2011.604600.

[28] S. Chesné, Indirect boundary force measurements in beam-like structures using a derivative estimator, Journal of Sound and Vibration 333 (24) (2014) 6438–6452. doi:10.1016/j.jsv.2014.07.026.

[29] S. Chesne, C. Pezerat, Distributed piezoelectric sensors for boundary force measurements in Euler–Bernoulli beams, Smart Materials and Structures 20 (7) (2011) 075009. doi:10.1088/0964-1726/20/7/075009.
[30] L. C. Pastrav, S. V. Jaecques, I. Jonkers, G. V. d. Perre, M. Mulier, In vivo evaluation of a vibration analysis technique for the per-operative monitoring of the fixation of hip prostheses, Journal of Orthopaedic Surgery and Research 4 (2009) 10. doi:10.1186/1749-799X-4-10.
[31] A. Preumont, Mechatronics: Dynamics of Electromechanical and Piezoelectric Systems, softcover reprint of hardcover 1st ed. 2006 édition Edition, Springer, 2011.
[32] A. Tijou, G. Rosi, R. Vayron, H. A. Lomami, P. Hernigou, C.-H. Flouzat-Lachaniette, G. Haïat, Monitoring cementless femoral stem insertion by impact analyses: An in vitro study, Journal of the Mechanical Behavior of Biomedical Materials 88 (2018) 102–108. doi:10.1016/j.jmbbm.2018.08.009.
[33] S. Chesne, C. Pezerat, Force identification by using specific forms of PVDF patches, Smart Structures and Systems 15 (2015) 1203–1214. doi:10.12989/sss.2015.15.5.1203.
[34] ANSI/IEEE, IEEE Standard on Piezoelectricity, ANSI/IEEE Std 176-1987 (1988). doi:10.1109/IEEESTD.1988.79638.